Real time imaging, forecasting and management of human-induced seismicity at Preston New Road, Lancashire, England

Authors: Huw Clarke[1], James P. Verdon[2], Tom Kettlety[2], Alan F. Baird[2], J-Michael Kendall[2]

1. Cuadrilla Resources Ltd., Cuadrilla House, 6 Sceptre Court, Bamber Bridge, Lancashire, U.K., PR5 6AW.

2. School of Earth Sciences, University of Bristol, Wills Memorial Building, Queen's Road, Bristol, U.K., BS8 1RJ.

ABSTRACT

Earthquakes induced by subsurface fluid injection pose a significant issue across a range of industries. Debate continues as to the most effective methods to mitigate the resulting seismic hazard. Observations of induced seismicity indicate that the rate of seismicity scales with the injection volume, and that events follow the Gutenberg-Richter distribution. These two inferences permit us to populate statistical models of the seismicity, and extrapolate them to make forecasts of the expected event magnitudes as injection continues. Here we describe a shale gas site where this approach was used in real time to make operational decisions during hydraulic fracturing operations.

Microseismic observations revealed the intersection between hydraulic fracturing and a pre-existing fault or fracture network that became seismically active. While "red light" events, requiring a pause to the injection program, occurred on several occasions, the observed event magnitudes fell within expected levels based on the extrapolated statistical models, and the levels of seismicity remained within acceptable limits as defined by the regulator. To date, induced seismicity has typically been regulated using retroactive Traffic Light Schemes. This study shows that the use of high quality microseismic observations to populate statistical models that forecast expected event magnitudes can provide a more effective approach.

1. Introduction

Human-induced seismicity is becoming an increasingly controversial topic. It is well known that activities such as mining and water impoundment can lead to felt seismicity, but increasingly activities such as geothermal energy (Grigoli *et al*., 2018), underground storage of waste such as CO_2 or water (Keranen *et al*., 2014), production from conventional hydrocarbon reservoirs (e.g. Segall, 1989) and hydraulic stimulation of shale gas reservoirs (Bao and Eaton, 2016), are attracting concern from the public, regulators and operators.

The stimulation of fractures by injecting water at high-pressure is a technique used to create conductive fracture networks in low-permeability reservoir rocks. Hydraulic fracture stimulation is widely used in the commercial production of hydrocarbons, and also to develop engineered geothermal systems. Use of this method has become more prominent in the past decade, associated primarily with the shale gas boom (Wang and Krupnick, 2013) in North America.

If hydraulic fractures intersect a pre-existing fault that is near to its critical stress state, the increase in pore pressure can reduce the effective normal stress, declamping the fault and creating induced seismicity. Such cases are relatively rare: Atkinson *et al*. (2016) estimate that only 0.3% of wells in British Columbia and Alberta, a region with some of the highest levels of hydraulic fracturing-induced seismicity (HF-IS), are associated with induced events larger than magnitude 3. Nonetheless, the issue of induced seismicity is a concern for the petroleum and geothermal industries, and will likely be of concern to other nascent industries, such as carbon capture and storage, as well (e.g., Verdon, 2014).

Debate continues with regards to the most effective methods to mitigate HF-IS, and what regulations should be applied. To date, regulators have typically imposed Traffic Light Schemes (TLSs) whereby the operator reduces, pauses or stops injection if the magnitude of the largest event exceeds a specified threshold. TLS thresholds have varied significantly in different jurisdictions (Bosman et al., 2006; Baisch et al., 2019): for example, in Alberta the red light is set at $M = 4$, whereas in the United Kingdom (U.K.) the red light is set at $M = 0.5$, a difference in earthquake moment of over 175,000 times.

The simple TLSs currently used by hydraulic fracturing regulators are essentially retroactive in nature, because the operator takes actions after an event has occurred. In some case studies, seismicity has been observed to continue, and increase in magnitude, after injection has ceased (e.g., Häring *et al*., 2008; Clarke *et al*., 2014). These post-injection increased-magnitude events, known as "trailing events", pose an issue for TLSs because they compel the regulator to set thresholds that may be substantially lower than the actual magnitude they wish to avoid. Hence operations may be stopped even though levels of seismicity are well below that which might be considered hazardous.

It is therefore desirable to manage and mitigate induced seismicity in real time, as operations proceed. For example, injection volumes or pressures could be reduced (e.g., Kwiatek et al., 2019), or stimulation can be directed away from areas showing fault reactivation. Here we show a successful example of managing HF-IS with a recently acquired dataset from a shale gas operation in the UK.

1.1 Using microseismic data for decision-making to mitigate induced seismicity

The TLSs described by Bosman et al. (2016) and Baisch et al. (2019) that are currently used to regulate hydraulic fracturing stipulate decisions based solely on the magnitude of the largest events. This is a rational option if monitoring is provided by national or regional seismometer networks, where monitoring stations may be 10s of km from the site (e.g., Clarke *et al*., 2014; Friberg *et al*., 2014; Skoumal *et al*., 2015; Schultz *et al*., 2015). In such cases only the larger events may be detected, and hypocentral locations and focal mechanisms may be poorly constrained. Hence the only reliable, well-constrained data are the magnitudes of the larger events.

However, it is not uncommon for operators to deploy microseismic monitoring, where downhole geophone arrays (Maxwell *et al*., 2010) or dense surface arrays (Chambers *et al*., 2010) are able to detect very low magnitude “microseismic” events. High-quality microseismic monitoring may record thousands or even hundreds of thousands of events with very precise locations, spanning several orders of magnitude, provided in real time during operations (e.g., Zinno et al., 1998). These data will be highly relevant for understanding the risks posed by HF-IS. However, such data is not utilized by the relatively simple TLSs currently being applied by hydraulic fracturing regulators (Bosman et al., 2016).

There are two primary ways by which microseismic observations can be used to guide decisions to mitigate induced seismicity. Firstly, microseismic data can be used to detect and characterise the interactions between hydraulic fractures and pre-existing faults (Maxwell *et al*., 2008; Maxwell *et al*., 2009; Wessels *et al*., 2011; Kettlety *et al*., 2019; Igonin *et al*., 2019; Eyre et al., 2019). Microseismic events during hydraulic fracturing typically occur in clusters extending from the well perpendicular to the minimum horizontal stress, tracking the growth of the hydraulic fractures and mapping the extent of the stimulated reservoir volume. If a fault is intersected events may begin to line up along the structure, allowing it to be identified and mapped (e.g., Maxwell *et al*., 2008; Wessels *et al*., 2011; Hammack *et al*., 2014; Kettlety *et al*., 2019 Igonin *et al*., 2019; Eyre *et al*., 2019). In many cases fault reactivation can also be identified by a decrease in Gutenberg and Richter (1944) *b* values (e.g., Maxwell *et al*., 2009; Verdon and Budge, 2018; Kettlety *et al*., 2019), or by an increase in the rate of microseismicity relative to the injection rate (e.g., Maxwell *et al*., 2008; Verdon and Budge, 2018).

If a fault is identified during injection, then an operator can re-design their injection program to avoid further interacting with the fault. This can be achieved, for example: by skipping stages along a horizontal well; by changing the planned injection rates or volumes; or by altering the properties of the injected fluid (for example a more viscous fluid will carry more proppant while travelling less distance into the formation). Alternatively, Hofmann *et al*. (2018) have proposed adopting a "cyclic soft stimulation" program, where repeated injection is conducted at significantly lower rates. Zang *et al*. (2019) have demonstrated this approach for experimental-scale injection tests. However, the results from application to an industrial-scale project (Hofmann *et al*., 2019) are more ambiguous, as the Pohang geothermal project, South Korea, at which this method was applied, went on to experience one of the largest injection-induced events ever recorded (Grigoli *et al*., 2018). Moreover, for shale gas hydraulic fracturing applications, it is not clear that such a low-rate injection program would result in effective proppant placement into a shale formation.

Microseismic data can also be used to make forecasts of the expected event magnitudes during stimulation. Induced seismicity has been observed to follow the Gutenberg and Richter (G-R hereafter) distribution (van der Elst *et al*., 2016), with the total number of events (Shapiro *et al*., 2010; Mignan *et al*., 2017) or the cumulative seismic moment released (Hallo *et al*., 2014) being scaled to the cumulative injection volume. As such, expected event magnitudes can be forecast by characterising these relationships for the site in question, and then extrapolating them to the planned injection volume. This approach has shown significant promise when applied in a pseudo-prospective manner (e.g., Verdon and Budge, 2018).

These concepts have produced more advanced approaches to mitigate induced seismicity. For example, Mignan *et al*., (2017) propose an adaptive Traffic Light Scheme (ATLS), whereby the daily rate of seismicity is scaled to the injection rate (as per Shapiro *et al*. (2010)), with the addition of a post-injection relaxation time that describes trailing effects. Event magnitudes are then determined from a G-R distribution, from which risk-based decisions can be made. Broccardo *et al*. (2017) extended the Mignan *et al*. (2017) approach by providing a

Bayesian framework within which the key parameters can be estimated. However, to our knowledge this approach has not yet been applied in real time to an active project.

Kwiatek *et al*. (2019) present an example of such methods being applied in real time to a deep geothermal project near Helsinki, Finland. They found that the observed seismicity scaled with injection parameters, allowing them to adjust the injection program to ensure that the levels of seismicity remained within the limits imposed by the regulator. The success of the type of approach demonstrated by Kwiatek *et al*. (2019), and the continued refinement of proposed adaptive TLSs (e.g., Mignan *et al*., 2017; Broccardo *et al*., 2017), provides the opportunity to move beyond the simple TLSs currently in common usage. However, their effectiveness must be demonstrated extensively in real time scenarios such that regulators gain confidence in their application.

1.2 A case study from northwest England

In this paper we report on the Preston New Road PNR-1z well, Lancashire, U.K., operated by Cuadrilla Resources Ltd (CRL hereafter). This was the first U.K. onshore well to be hydraulically fractured since a government review of HF-IS seismicity was concluded in 2012. As such it is the subject of regular national media attention (e.g., Webster, 2018) and debate in the national parliament (Hansard, 2018). Given the high levels of public scrutiny, the site was extensively monitored both by CRL, and by independently-funded organisations such as the British Geological Survey (BGS). This monitoring included groundwater, surface water, air quality, and traffic movements, as well as the induced seismicity monitoring described here. Extensive baseline surveys were conducted for all of the above, so that any change from the pre-operational conditions could be identified.

Given public concerns about HF-IS in the U.K., CRL took proactive measures to mitigate induced seismicity, guided by microseismic observations as outlined above. Here we provide a brief description of the operations conducted at the site, then show how microseismic data were used to identify and map the interaction between hydraulic fractures and a fault, and to forecast expected event magnitudes as the injection progressed. This information allowed CRL to adjust their injection program, ensuring that levels of seismicity did not exceed the overall objectives set by the regulator, as well as providing an increased understanding of more proactive measures that could be applied in future as alternatives to simplistic TLSs.

2. Description of the Preston New Road Site

The Preston New Road PNR-1z well targets the Carboniferous Lower Bowland Shale at a depth of approximately 2,300 m. The lateral portion of the well extends 780 m in a westward direction (Figure 1). A sliding-sleeve completion was used, with 41 individual sections spaced at 17.5 m intervals. CRL planned to stimulate each of these sleeves with 400 m^3 of slickwater, placing 50 tonnes of proppant per sleeve. Stimulation was carried out in two periods (Figure 2), firstly from 15th October to 2nd November, and then from 8th to 17th December 2018.

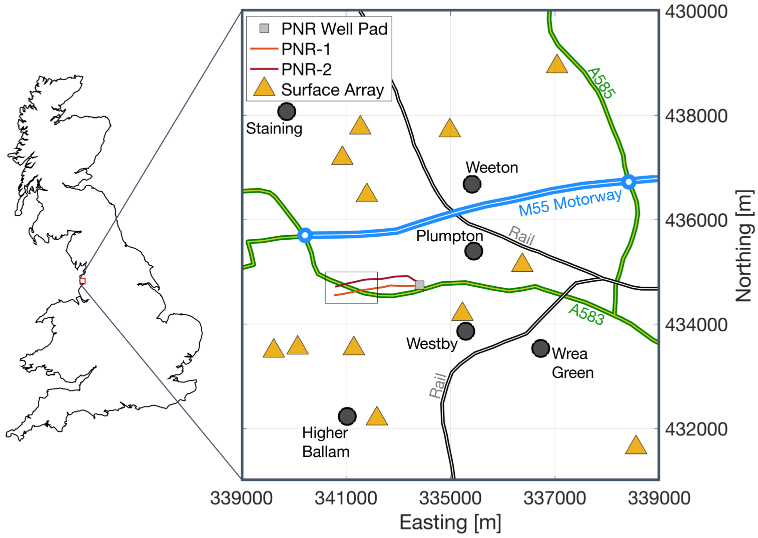

Figure 1: Map of operations at Preston New Road showing the positions of the drilling pad and horizontal tracks of PNR-1z and PNR-2, and the positions of the surface monitoring stations. The black box marks the area of interest shown in subsequent figures. Major roads, rail links, and nearby villages are also marked. Coordinates are U.K. Grid Reference.

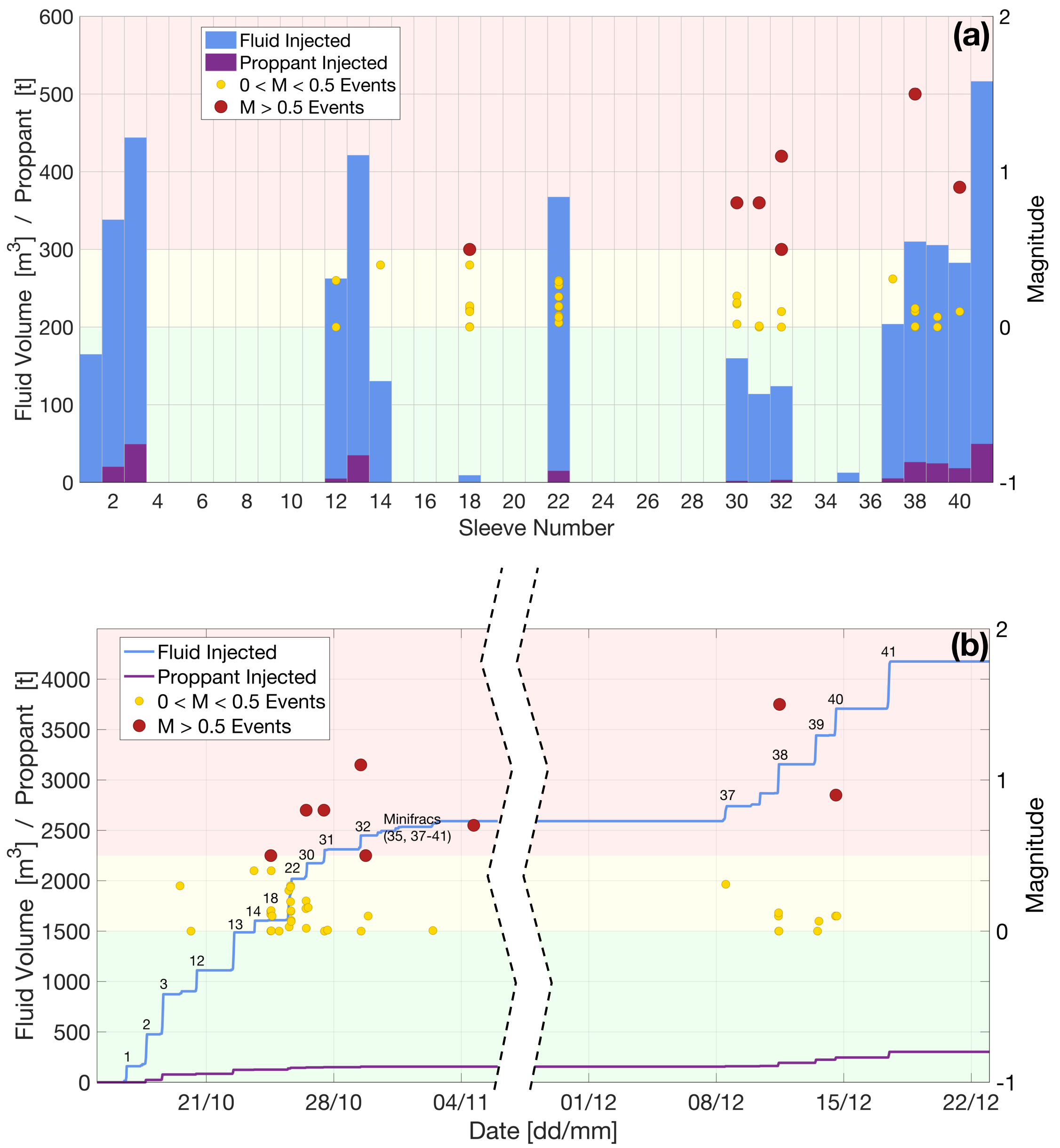

Figure 2: Overview of injection into PNR-1z. (a) shows the volume of fluid (blue) and mass of proppant (purple) injected into each sleeve. It also shows all M > 0 TLS events (yellow and red dots) that occurred during or after injection into each sleeve. (b) shows cumulative fluid volume (blue) and proppant mass (purple) injected as a function of time, again showing the occurrence of TLS events. The numbering in (b) shows the sleeve being injected. The background colours show the TLS green, amber and red magnitude thresholds.

2.1 U.K. Regulations for Induced Seismicity

In the U.K., HF-IS is regulated by the Oil and Gas Authority (OGA). The OGA's objective is to minimize the number of events felt at the surface by the public, and to avoid the possibility of events capable of causing damage to nearby buildings or infrastructure (Oil and Gas

Authority, 2018). U.K. standards for ground vibrations from other activities such as quarry blasting, construction equipment and industrial machinery are provided by British Standard BS 7385-2. This sets a peak ground velocity (PGV) threshold, above which may cause cosmetic damage such as cracking of plaster, of 15 mm/s (at lower frequencies such as would be expected from induced seismicity). Using ground motion prediction equations (Akkar *et al.,* 2014), for hypocentral depths equivalent to expected depths of hydraulic fracturing and making conservative assumptions for ground conditions, this threshold is approximately equivalent to a magnitude of $M = 3.5$. Therefore, the OGA's objective could be reasonably translated as minimizing the number of events that have magnitudes $2 < M < 3$, and avoiding events that have magnitudes $M > 3.5$.

To regulate HF-IS the OGA currently applies a TLS with a red-light threshold of $M = 0.5$ (Green *et al*., 2012), for which the operator must stop injection, reduce the pressure in the well, perform well integrity checks, and wait at least 18 hours before resuming injection. This is by some margin the most stringent level for ground motion applied to any industrial activity that we are aware of. The $M = 0.5$ red-light threshold is 175 times smaller than the $M = 2$ events that the scheme seeks to minimize, and over 30,000 times smaller than the $M > 3.5$ events that the scheme seeks to avoid. This disparity exists to mitigate the risk posed by trailing events, where event magnitudes may continue to increase after injection has been stopped (see Mignan *et al*. (2017) for an attempt to forecast trailing event populations). This TLS was applied to stimulation of the PNR-1z well, and the restrictive nature of this scheme had a significant impact on the operations: only 17 of the planned 41 stages were injected, and of these only 2 injected the 50 tonnes of proppant that was planned. However, only 2 events were reported by the British Geological Survey (BGS) as being felt, and ground motions remained well below the levels at which damage might be expected. Therefore, overall the operation complied with the regulator's objective to minimise felt seismicity and avoid damaging seismicity.

2.2 Real time seismic and microseismic monitoring

Two systems were used in combination to monitor induced seismicity at Preston New Road. Both of these systems provided event locations and magnitudes in real time (typically within 1-4 minutes of event occurrence) computed by a processing contractor (Schlumberger). To administer the TLS an array of 8 sensors including 2 broadband seismometers and 6 geophones (4.5 Hz instruments) was deployed at the surface, augmented by 4 broadband seismometers deployed by the BGS (Figure 1). During real time monitoring the surface array identified 54 events with a minimum magnitude of $M_L = -0.8$. The surface array provided sufficient coverage such that focal mechanisms could be determined for 9 of the largest events during real time monitoring.

Microseismicity was recorded using an array of 24 geophones (15 Hz instruments) placed in the build section (where the well deviates from vertical to horizontal) of the adjacent PNR-2 well, 200 m shallower and 220 m northeast of the nearest sleeve in PNR-1z (Figure 3). This array reported over 39,000 events in real time, with a minimum magnitude of M_W = -3.0.

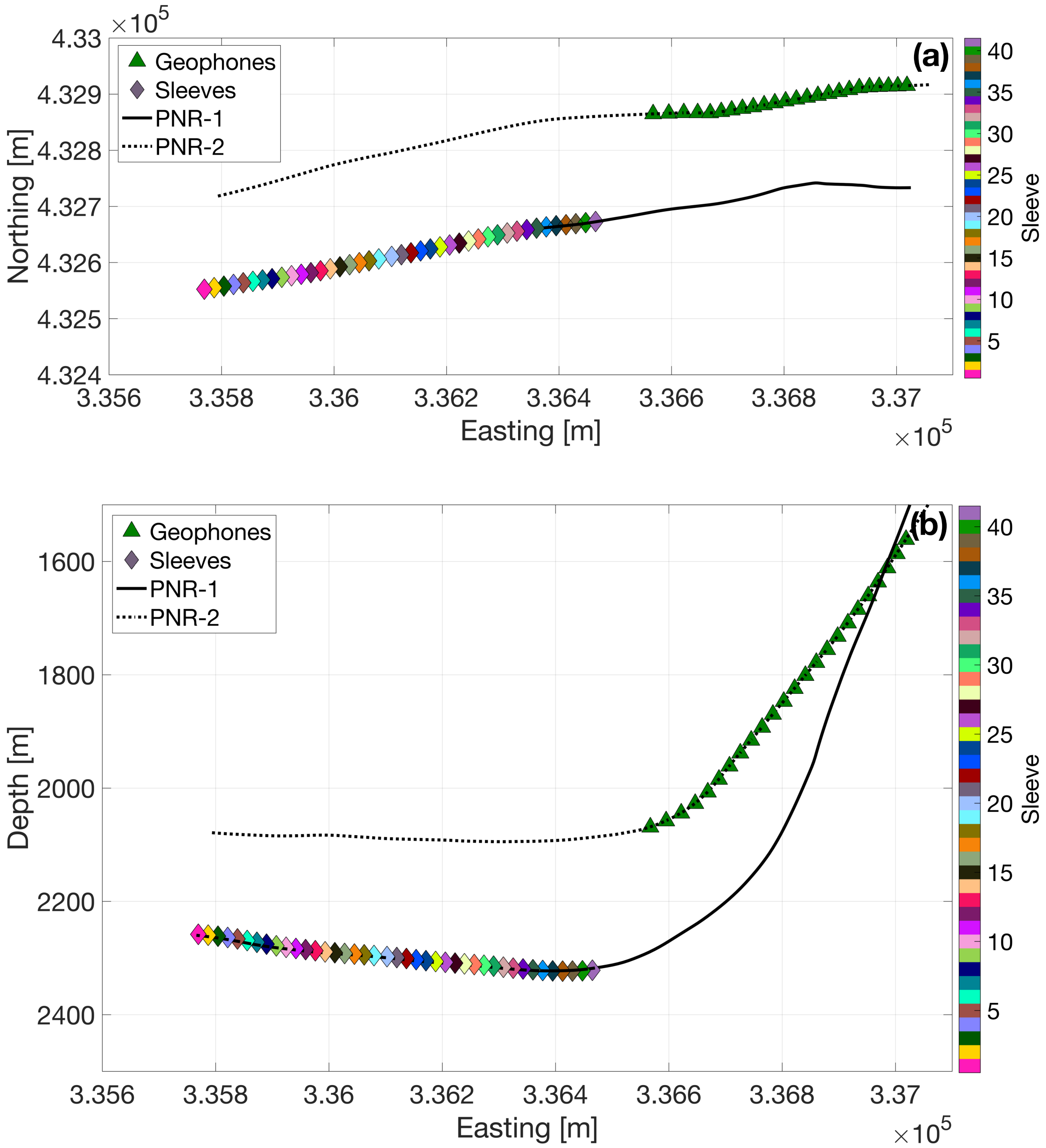

Figure 3: Map (a) and cross-section (b) of the downhole monitoring array deployed in well PNR-2, and the sleeves through which injection was conducted in PNR-1z.

2.3 A note on magnitudes

Measurements of magnitudes for small events can be challenging (Kendall *et al.,* 2019). Two different magnitude scales were in use during real time operations at Preston New Road. The U.K. TLS regulations mandate the use of a local magnitude scale with a correction applied to account for the small source-receiver distances (Butcher *et al*., 2017; Luckett *et al.,* 2019). Therefore, magnitudes from the surface array were reported as M_L values. However, these M_L scales are calibrated using surface stations, implicitly including free-surface effects and near-surface attenuation, so this M_L scale is not calibrated for downhole instruments. Instead the downhole events were reported as M_W values. While a direct comparison and conversion between the two scales might seem like an obvious solution (e.g. Edwards and Douglas, 2014), in practice this was more challenging. The surface array recorded the largest 54 events, so only these events had reported M_L values. However, many of these larger events produced subsurface motions that were beyond the dynamic range of the downhole instruments, and so accurate downhole M_W values could not be determined for these events. Hence, there is only a small subset of events which are large enough such that a robust M_W value can be computed using the surface array, but no too large such that a robust M_W value can also be computed using the downhole stations, thereby enabling a comparison to be made.

Work is ongoing to resolve the observed M_L and M_W values. However, the need for rapid decision-making meant that this information was not used during real time operations. Instead, we used M_L values for the 54 events that were reported by the surface array, and M_W values for the remaining events. Clearly this solution was far from optimal. However, we note that doing so does not produce anomalies or unusual behaviour if the overall magnitude-frequency distribution is examined (Figure 4), suggesting that this approach was reasonable in this case. However, in future cases this issue should be addressed by ensuring that moment magnitudes are reported by both array types, and that relationships to convert between downhole M_W values and surface M_L values are calibrated. In Figure 4 we fit a G-R distribution to entire event catalogue using the Aki (1965) maximum likelihood approach, computing the magnitude of completeness, M_{MIN}, using both the Wiemer and Wyss (2000) formulation with an acceptance threshold of 95%, which gave M_{MIN} = -0.95, and by using a Kolmogorov-Smirnov test with a 10% significance threshold (e.g., Clauset *et al*., 2009; Williams and Le Calvez, 2013), which gave M_{MIN} = -0.8. In both cases, the resulting G-R parameters were a = 1.9 and b = 1.3.

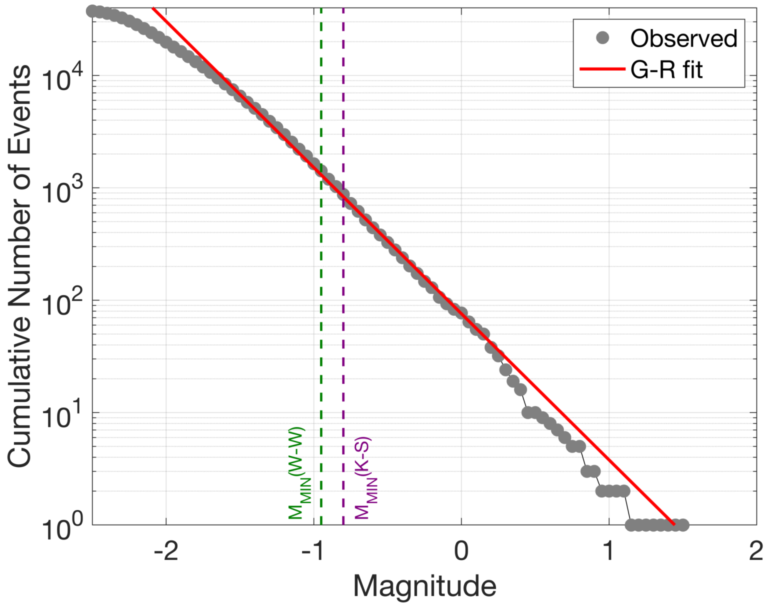

Figure 4: Magnitude-frequency distribution for all events reported in real time (grey dots). The observed distribution follows the G-R distribution with a = 1.9 and b = 1.3 (red line). We use both the Wiemer and Wyss (2000) formulation (green dashed line) and a Kolmogorov-Smirnov test (purple dashed line) to assess the overall magnitude of completeness.

3. Microseismic observations

Figure 5 shows a map and cross-section for located events with a signal-to-noise ratio greater than 5. Events during each stage are mostly found in the vicinity of the corresponding injection sleeve, extending approximately 200 m to the north. The events extend approximately 150 m above and below the well, remaining within the Bowland Shale Formation. The largest observed event has a magnitude of $M = 1.5$, and in total 8 events exceeded the TLS $M = 0.5$ threshold, 3 of these occurred during injection and required pumping to be stopped, while the remaining 5 were trailing events that occurred after injection had ceased.

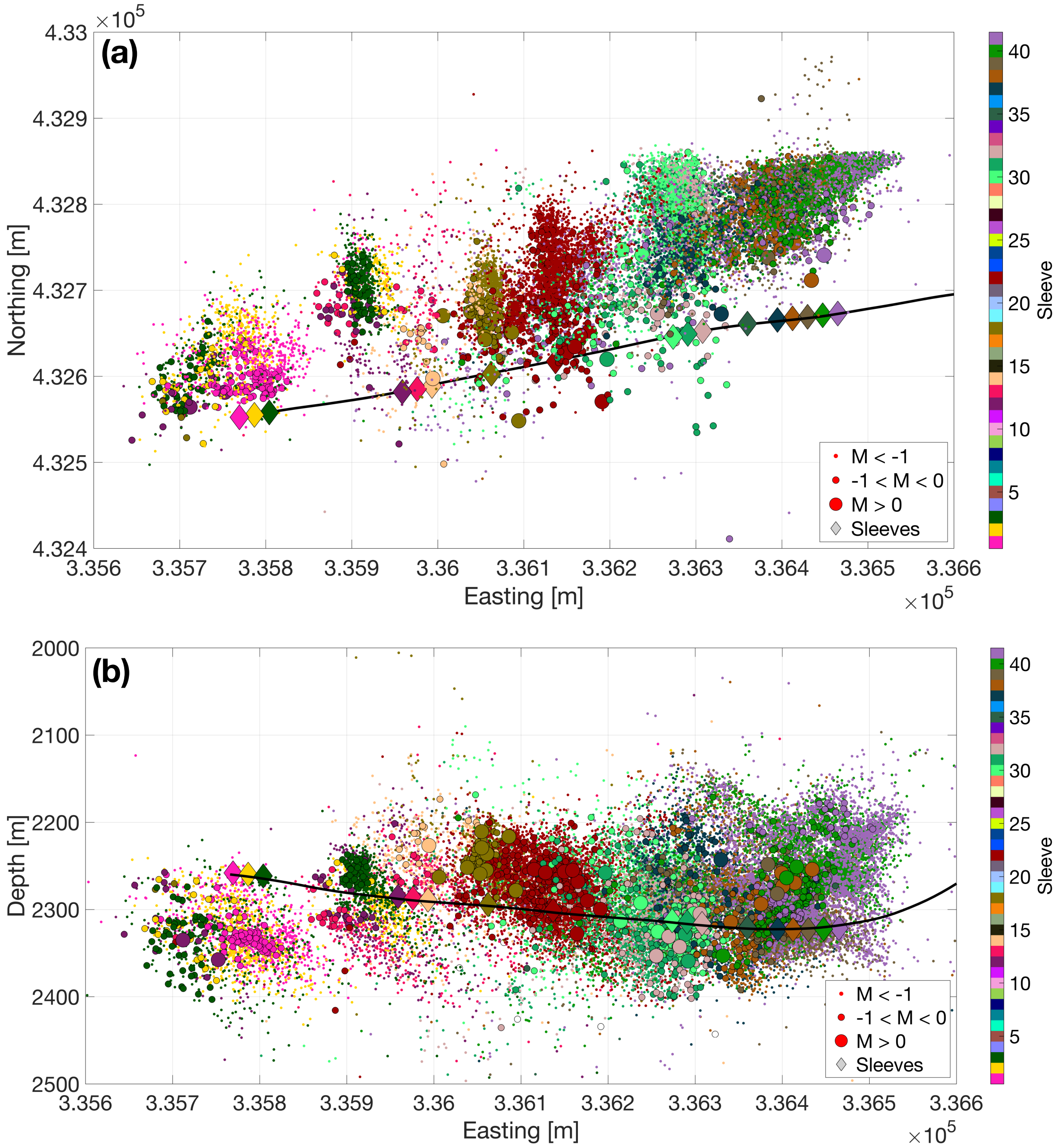

Figure 5: Map view (a) and cross-section (b) of microseismic events detected during real time monitoring at PNR-1z. Events are coloured by the sleeve number with which they are associated. The PNR-1z well profile is shown by the black line.

3.1. Relationship between microseismicity and previously-observed faults

Prior to the start of operations, a 3D reflection seismic survey was acquired at the site. Several pre-existing faults and "seismic discontinuities" (potential small faults that are at the limit of resolution for 3D seismic surveys) were identified (Cuadrilla Resources Ltd., 2018). We observed little or no correlation between the positions of these features the and microseismicity. The events associated with Stages 1 – 3 at the toe of the well overlap with one of the seismic discontinuities. However, the levels of microseismicity produced by these stages were among the lowest. In contrast, none of the events that exceeded the $M > 0.5$ TLS threshold occurred on structures identified from the 3D survey.

Indeed, no microseismicity coincided with any of the large faults identified in the 3D seismic survey, all of which were significantly further from the well than the greatest distances reached by the microseismicity. This observation allowed CRL to proceed with confidence that the hydraulic stimulation was unlikely to cause re-activation of the larger faults that had been identified.

3.2. Identification of potential seismogenic structures

The northwards propagation of microseismicity from each injection sleeve traces the propagation of hydraulic fractures perpendicular to the minimum horizontal stress azimuth of approximately 80° (Fellgett et al., 2017). However, our interest was to identify pre-existing structures on which the larger events may occur. We note that the largest event, with a magnitude of $M = 1.5$, could correspond to a rupture with displacement of less than 1 cm with a length less than 100 m. At this scale the distinction between a “small fault” and a “large fracture” is somewhat arbitrary: we will use “fault” hereafter to describe such features, while keeping this fact in mind.

In Figure 5 the events do not display an obvious alignment along a pre-existing fault, an observation which often provides the clearest evidence of fault reactivation (e.g., Igonin *et al.*, 2019; Kettlety *et al.*, 2019; Eyre *et al.*, 2019). Instead, we use a combination of observations to identify and define the seismogenic structures responsible for the largest events.

3.3. Focal mechanisms

The focal mechanisms for 6 of the largest events are shown in Figure 6a. The events all have similar mechanisms: either left-lateral strike slip on a near-vertical fault striking NE-SW, or right-lateral strike-slip on a near-vertical fault striking NW-SE. The consistent orientation of these focal mechanisms provides a constraint for the orientation of any potential seismogenic structure.

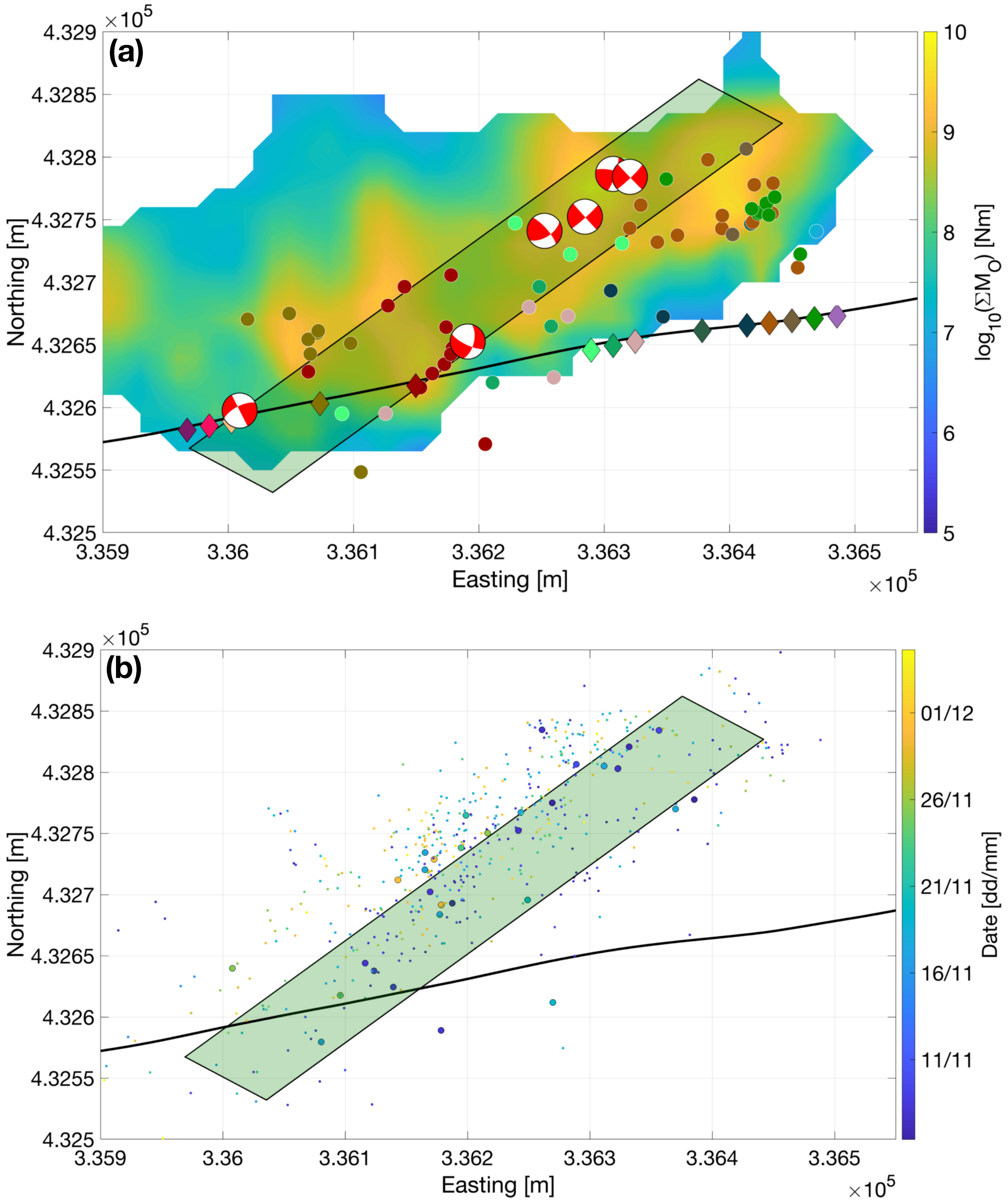

Figure 6: Maps showing the observations used to identify seismogenic structures. (a) shows all events with M > 0 (dots coloured by sleeve number as per Figure 5), the cumulative seismic moment (contours), and the focal mechanisms of the largest events. (b) shows a map of the events that occurred during the injection hiatus from 3rd November to 7th December. We combine the largest events and the injection hiatus events to map a plane striking at 237º and dipping at 70º (black-outlined box).

3.4. Mapping large events and cumulative moment release

Figure 6a also shows the positions of all events with $M > 0$, and maps the cumulative seismic moment release, ΣM_O. These observations allow us to identify a single zone in which almost all of the larger events were occurring, and within which the overall cumulative seismic moment release was highest. This zone intersects the PNR-1z well at roughly the position of Sleeve 18, which was the first stage on which an event exceeding the $M > 0.5$ TLS threshold occurred. Interaction between injection activities and this zone occurred along the well towards the heel. Importantly, the orientation of this zone matches the orientation of the NE-SW plane of the observed focal mechanisms.

3.5. Microseismicity during injection hiatus

These observations allowed us to identify the seismogenic feature during the initial stimulation of Stages 18 – 41 in October 2018 (Figure 2). From the 3rd of November, CRL paused the injection program in response to repeated $M > 0.5$ events that had occurred during the previous week. The injection pause continued until 7th December. Observations of microseismicity during this injection hiatus (Figure 6b) provided the final and definitive identification of the seismogenic structure. The events during hiatus, almost all of which had magnitudes less than $M < -1$, were all located along the same feature that we had identified from the focal mechanism orientations, the positions of the largest events, and the cumulative moment release map.

Our overall interpretation of the observed microseismicity is that a pre-existing fault plane runs northeast from the well. During hydraulic stimulation, larger events occurred when the hydraulic fractures from each stage intersected this fault. During the hiatus, whereas the microseismic events associated with hydraulic fracturing stopped, low levels of microseismicity continued to persist along this feature for a longer period of time. We fit a plane to a combined population of the $M > 0$ events (Figure 6a) and the hiatus events (Figure 6b), by finding the plane that minimises the least-squares distance between each event and the plane. We found a strike of 237° and a dip of 70°, which is consistent with the observed focal mechanisms. We term this fault NEF-1 (Northeast Fault-1) hereafter. With the maximum and minimum horizontal stresses oriented north-south and east-west respectively, this plane is well-oriented for the observed left-lateral strike slip motion, and the observed focal mechanisms are therefore consistent with the local stress conditions.

4. Statistical Forecasting of Event Magnitudes

During stimulation we applied in real time an event magnitude forecasting model to guide operational decisions with respect to induced seismicity. Hallo *et al*. (2014) introduced the concept of seismic efficiency, S_{EFF}, which describes the correlation between the cumulative moment release, ΣM_O, and the cumulative injection volume ΔV:

$$S_{EFF} = \frac{\Sigma M_O}{\mu \Delta V}, \tag{1}$$

where μ is the shear modulus, assumed to be 20 GPa here. Based on the observed values of S_{EFF} and the *b* value, the size of the largest expected event, M_{MAX} can be estimated as:

$$M_{MAX} = \frac{2}{3}\left(\log_{10}\left(\frac{S_{EFF}\mu\Delta V\left[\frac{3}{2}-b\right]}{b 10^{9.1}}\right)\right) + \frac{2}{3}\log_{10}\left(10^{b\delta} - 10^{-b\delta}\right), \tag{2}$$

where δ is the probabilistic half-bin size defined around M_{MAX} (Hallo *et al*., 2014). This formulation assumes that *b* and S_{EFF} do not change significantly for a given stage, or for a given volume of rock being stimulated. Verdon and Budge (2018) applied this approach in a pseudo-prospective manner to a hydraulic fracturing dataset from the Horn River Shale, Canada, showing that it would have accurately forecast event magnitudes had it been applied in real time.

Equation 2 posits a logarithmic dependence between injection volume and the largest event size. Given that the planned injection volumes do not vary by orders of magnitude between stages, the primary controlling factor on the largest event magnitude is therefore S_{EFF}. The relationship between S_{EFF}, ΔV, and M_{MAX} is plotted in Figure 7 (assuming *b* = 1).

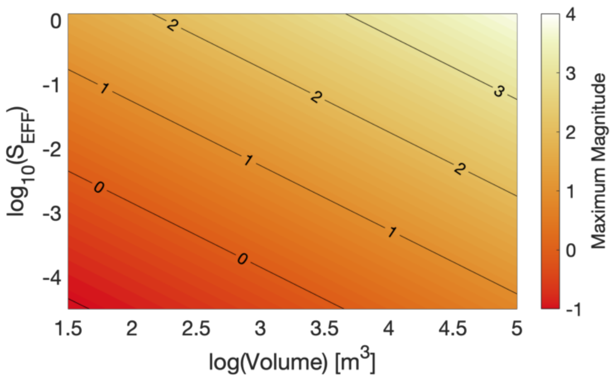

Figure 7: Relationship between S_{EFF}, ΔV, and M_{MAX} given by Equation 2 (assuming b = 1), showing the logarithmic dependence of M_{MAX} on ΔV.

Equation (2) provides the most likely maximum event magnitude. In practice it is more useful to define a value for M_{MAX} that is unlikely to be exceeded. Using synthetic event distributions, Verdon and Budge (2018) showed that adding a value of 0.5 to Equation 2 is sufficient to capture 95% of the variance between true and re-constructed model populations. In our analysis we applied this correction such that our results provided a value that, within reasonable levels of certainty, will not be exceeded.

We tracked b and S_{EFF} in real time during every stage, providing regularly-updated forecasts of M_{MAX}. We computed the b value using the Aki (1965) maximum likelihood approach, finding the minimum completeness threshold using a Kolmogorov-Smirnov test at a 10% acceptance level to assess the quality of fit between the observed magnitude distribution and the G-R relationship (Clauset *et al*., 2009; Williams and Le Calvez, 2013), requiring a minimum of 50 events for a reliable measurement (though with over 39,000 events in 17 stages, the number of events passed this threshold very quickly for each stage).

Figure 8 shows a selection of results for this analysis when performed on a stage-by-stage basis, i.e., considering ΣM_O and ΔV associated with each individual stage. We find that for most of the stages this approach provided accurate bounds, with the observed events falling within the modelled value of M_{MAX}. However, this is not always the case, as can be seen for Stages 32 and 38 in Figure 9, for example.

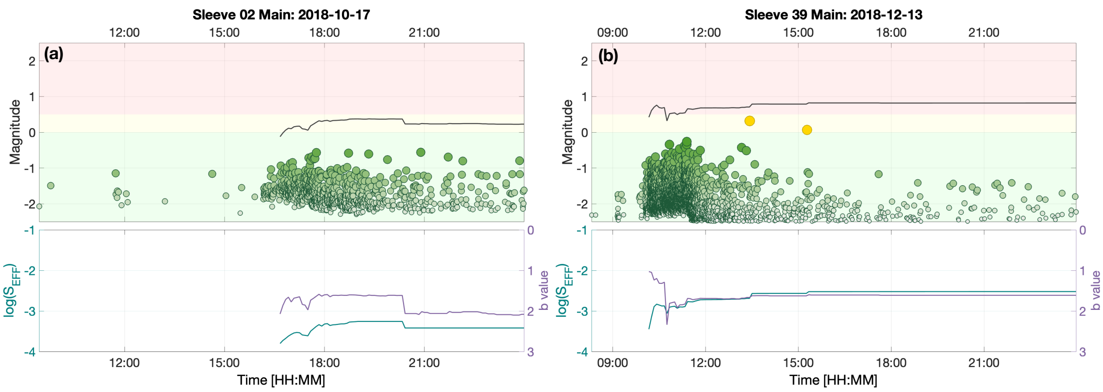

Figure 8: Examples of S_{EFF}, b, and M_{MAX} tracked during injection on a stage-by-stage basis. In the lower panels we track S_{EFF} (blue) and b (purple), and in the upper panels we plot the resulting values of M_{MAX} (black line) compared against observed events (circles coloured by magnitude relative to the TLS thresholds).

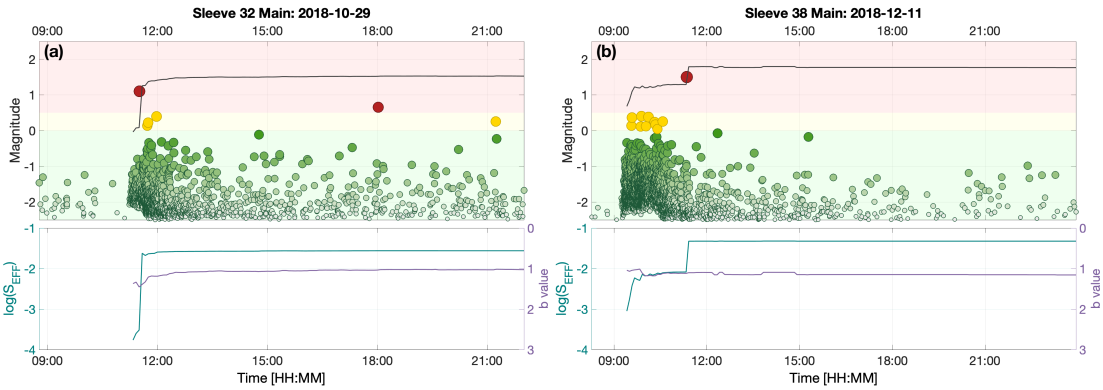

Figure 9: Examples of S_{EFF}, b, and M_{MAX} tracked during injection on a stage-by-stage basis, in the same format as Figure 8. For some stages, events occur that exceed the modelled M_{MAX} values, when the injection volumes and observed events are treated discretely on a stage-by-stage basis.

The reason for this discrepancy is obvious when considered in the light of the observations and interpretations of the microseismicity presented in Section 3: the NEF-1 fault runs obliquely to the well and was intersected by multiple stages. It is therefore not appropriate to consider each stage independently because the seismicity was caused by repeated injection into the same feature. Instead, as the NEF-1 feature was identified, we adjusted our approach to include the effects of repeated injection, treating all injection and seismicity from Stage 18 onwards cumulatively (Figure 10a). The value of S_{EFF} was observed to stabilise very quickly at a value of approximately $\log_{10} S_{EFF} \approx -2$, which produces a forecast M_{MAX} of 1.7. The largest observed event at PNR-1z had a magnitude of M = 1.5.

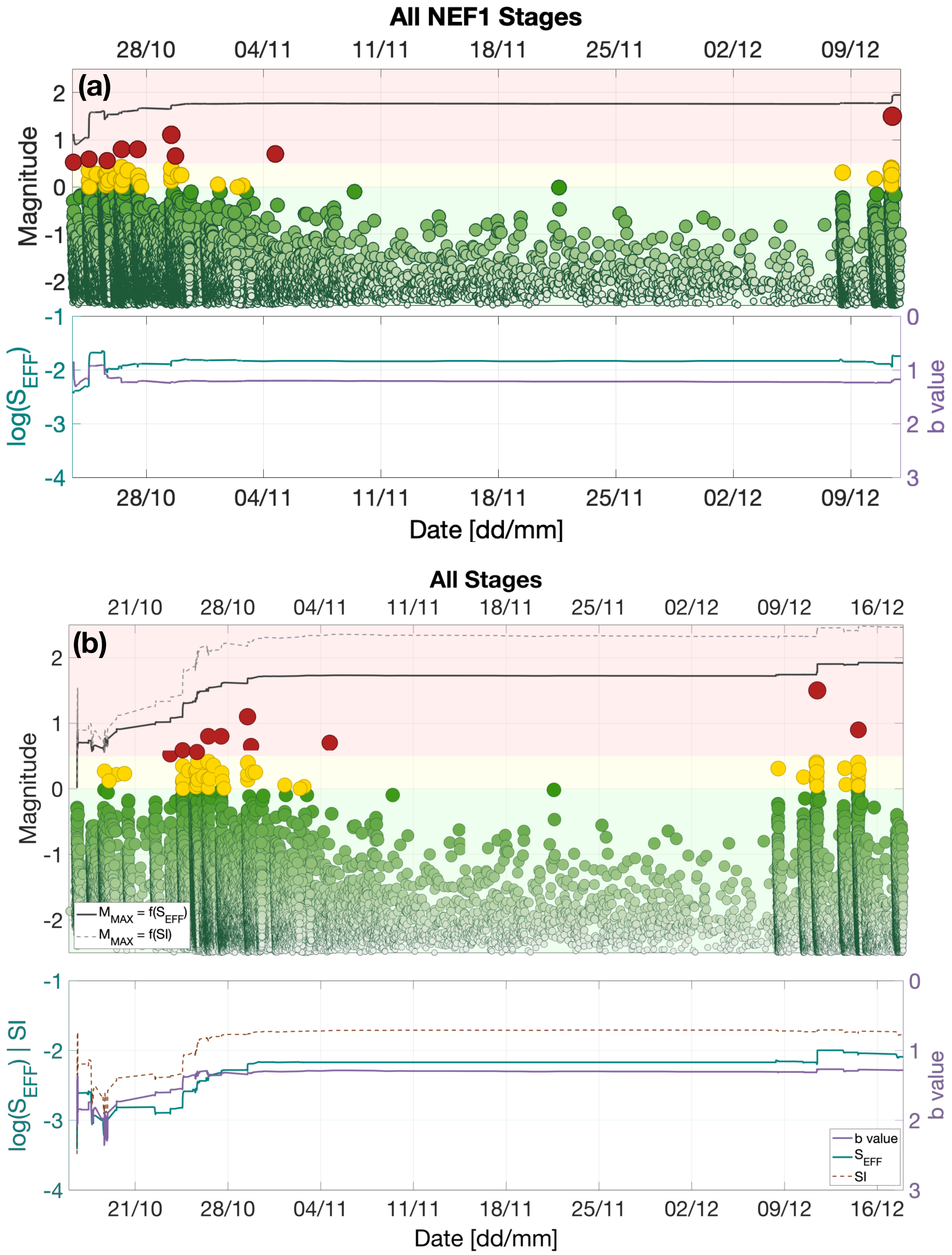

Figure 10: Forecasting M_{MAX} over cumulative stages. Here we treat stages cumulatively to generate M_{MAX} forecasts when (a) all of the stages that intersect the NEF-1 fault are considered, and (b) when all stages are considered. The observed S_{EFF} is initially at approximately $log_{10} S_{EFF} \approx -3$, giving a forecast $M_{MAX} < 1$. As the injection begins to interact with the NEF-1 feature, the b value decreases and the overall seismic efficiency increases to approximately $log_{10} S_{EFF} \approx -2$, giving a forecast $M_{MAX} < 2$. In (b) we also

show the Shapiro et al. (2010) seismogenic index (gold dashed line), and the resulting M_{MAX} forecast from this approach (grey dashed line).

For completeness, we also considered the cumulative impacts of the full injection volume and seismicity from all the injection stages (Figure 10b). This represents the worst-case scenario if all of the injected fluid was inducing events on a single seismogenic feature. Initial values for S_{EFF} are low ($\log_{10} S_{EFF} \approx -3$) and *b* values are high (*b* > 1.5) giving $M_{MAX} < 1$. From Stage 18 onwards we observed the hydraulic fracturing interact with the NEF-1 fault, producing an increase in S_{EFF} to ($\log_{10} S_{EFF} \approx -2$) and a decrease in *b* to approximately 1. This produces an increase in M_{MAX} to $M_{MAX} \approx 2$.

5. Discussion

5.1. Operational Decision-Making

The observations presented above were used by CRL to guide their operational decision-making, especially during the latter injection stages in December, after the period of injection hiatus in November 2018.

During hydraulic fracturing, placement of the proppant cannot begin until fracture breakdown has occurred and fractures begin to propagate. This typically requires a minimum of approximately 80 m^3 of fluid. The proppant concentration is then gradually increased as the injection continues, such that the majority of proppant is placed at the end of the stage. If a stage is terminated mid-way through by a TLS red-light event, only a small proportion of the proppant will have been placed, even if several hundred m^3 of fluid has been injected. In effect, the stage will therefore have been wasted and the environmental water use and seismic risk unnecessarily increased.

At PNR-1z, the modelling described above showed that events larger than *M* = 2 were not expected on the NEF-1 fault given the observed *b* values and seismic efficiency, and the planned injection program. This forecast was reported to the OGA in November 2018, and it falls within the objectives of seismicity mitigation set out by the OGA (minimising felt events and avoiding damaging events). However, the NEF-1 fault could be expected to continue producing *M* > 0.5 red-light events that would terminate injection, preventing the placement of proppant. CRL therefore decided that further injection into the sleeves that intersect the NEF-1 fault would be wasted, and in December 2018 they restarted injection in Stages 37 – 41 at the heel of the well. Based on the seismicity mapping described in Section 3 it was hoped that these stages would pass to the east of the NEF-1 fault, allowing stages to be completed without interruption. Based on the forecasting described in Section 4, CRL was able to do so with confidence if these stages did intersect NEF-1, the levels of seismicity would not exceed the objectives set by the OGA, and therefore injection could be conducted safely.

In reality, some of these latter stages did intersect the NEF-1 fault, triggering two further TLS events with $M > 0.5$. However, the event magnitudes remained within the levels that had been forecast, as described in the section above, and within the overall regulatory objective to minimise the number of felt events.

5.2. Seismic Efficiency and Seismogenic Index

The Seismogenic Index, *SI* (Shapiro *et al.*, 2010), is another parameter that is commonly used to describe the relationship between injected volume and seismicity. Whereas the S_{EFF} parameter we use here scales the injection volume to the cumulative seismic moment release, the seismogenic index scales the injection volume to the number of events larger than a given magnitude. Since many previous studies have provided estimates of *SI*, it is of interest to compute this parameter for the PNR-1z dataset to facilitate a comparison. Our results are shown alongside the S_{EFF} results in Figure 10, and we also plot the M_{MAX} forecasts that result (at 5% probability of exceedance level) using the method described by Shapiro *et al.* (2010). We note that, as found by Verdon and Budge (2018), *SI* follows a similar trend to $\log_{10} S_{EFF}$, which is not surprising because the total moment release will depend on the number of events that occur. We also find that the M_{MAX} values derived from the *SI* measurements are larger than those derived from the S_{EFF} measurements, as also found by Verdon and Budge (2018).

Dinske and Shapiro (2013) catalogue *SI* values for a range of injection sites, finding values ranging from $-9 < SI < 1$. The maximum value of *SI* obtained here is $SI = -1.8$, which is similar to many of the geothermal projects described by Dinske and Shapiro (2013), but significantly larger than those obtained for hydraulic fracturing sites at Cotton Valley (East Texas) and in the Barnett Shale (Northeast Texas). However, the values obtained for PNR-1z are similar to values found by Verdon and Budge (2018) for hydraulic fracturing in the Horn River Basin, British Columbia, Canada, where $-4 < SI < -1$, and towards the lower end of the range found by Schultz *et al.* (2018) for hydraulic fracturing sites in Alberta, Canada, where $-2.5 < SI < -0.5$. The most notable past case of injection-induced seismicity in the U.K. for which *SI* values are available is the Rosemanowes Hot Dry Rock geothermal site, for which Li *et al.* (2018) found maximum values of $SI = -3.4$, significantly lower than the values found for PNR-1z.

5.3. Scaling between volume and cumulative moment release

The underlying assumption implicit to Equation (1) is that the cumulative seismic moment scales linearly with the injection volume. However, recent studies (e.g., Galis *et al.*, 2017; De Barros *et al.*, 2019) have proposed alternative scaling factors, and in particular that

$$\Sigma M_O \propto V^{\frac{3}{2}}. \qquad (3)$$

This scaling by an exponent of 1.5 is also implicit to the Shapiro *et al.* (2010) *SI* approach, since the logarithm of the seismic moment scales with 1.5 × M_W. Discussion continues as to the most appropriate value of the scaling exponent between ΣM_O and V (e.g., Chen *et al.*, 2018; De Barros *et al.*, 2019).

In Figure 11a we track the evolution of the cumulative moment release with the cumulative injection volume, and estimate a least-squares fit (in log-log space) to these data for a relationship having the form

$$\Sigma M_O = \alpha V^n. \qquad (4)$$

Our results are shown in Figure 11a. For the overall dataset, we find a best-fit value of n = 1.6. However, it is apparent that the data may not be best described by a single value. Based on our observations of which stages caused reactivation of the NEF-1 fault, combined with apparent changes in slope of Figure 11a, we divide the data into 3 periods: Stages 1 – 14, prior to reactivation of the NEF-1 fault; Stages 18 – 38, while reactivation of the fault was taking place, and Stages 39 – 41 which appeared to miss the NEF-1 fault at the heel of the well. Doing so, we find best-fit values of n = 0.8 for Stages 1 – 14; n = 3.0 for Stages 18 – 38, and n = 0.6 for Stages 39 – 41.

This variability highlights a challenge that arises when attempting to assess any scaling relationship between cumulative moment and volume, should the constant of proportionality (α in Equation (4)) vary during the process, which might be expected as hydraulic fracturing proceeds along a horizontal well, and so encounters different volumes of rock that have different geomechanical properties.

We further demonstrate this effect in Figure 11b. Based on our observations in Section 4, we simulate a scenario whereby event populations are generated with b = 1.2 and $\log_{10} S_{EFF}$ = -2.6 (assuming a linear relationship between V and ΣM_O) for the first 1,600 m^3 of injection (representing Stages 1 – 14); $\log_{10} S_{EFF}$ = -1.7 for the second 1,500 m^3 of injection (representing Stages 18 – 38); and $\log_{10} S_{EFF}$ = -2.7 for the final 1,100 m^3 of injection (representing Stages 39 – 41). Events are generated stochastically to meet these criteria, and are assumed to occur at random times within each of the specified periods. We generate 1,000 such populations, and in Figure 11b we plot the median value of ΣM_O as a function of V, and the boundaries containing 95% of the models. The resulting models show good agreement with the observed evolution of cumulative moment release.

This modelling indicates the need for caution when attempting to constrain the relationship between moment release and volume: if the constant of proportionality varies during injection then a simple comparison of moment and volume may lead to under- or overestimates of the exponent n. For this dataset, a linear relationship between cumulative moment and volume, with an increase in S_{EFF} from $\log_{10} S_{EFF}$ = -2.6 to $\log_{10} S_{EFF}$ = -1.7 during reactivation of the NEF-1 fault, provides a good fit to the observed seismicity.

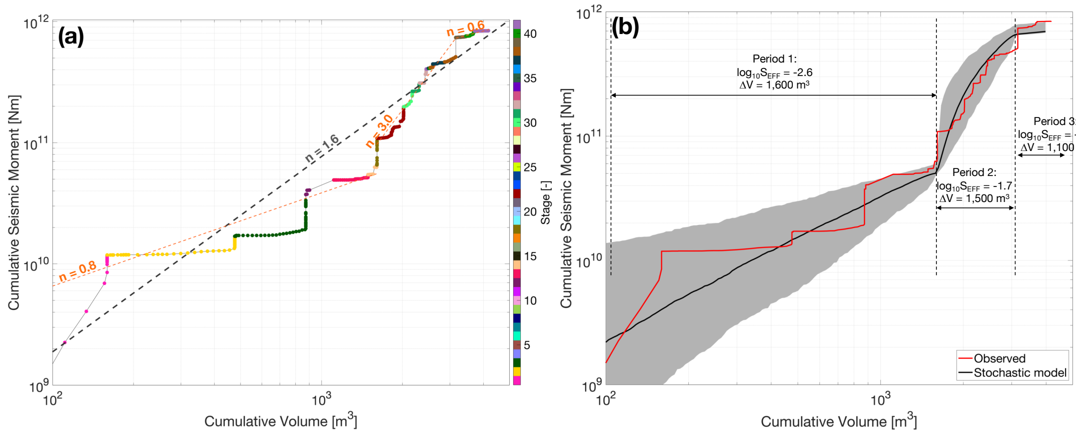

Figure 11: Evolution of cumulative seismic moment with injection volume. In (a), data points are coloured by the corresponding stage. Power law fits to the observations are shown, with a best-fit exponent of n = 1.61 for the overall dataset (dark grey dashed line), but n = 0.77 for the early stages, n = 2.98 where the NEF-1 reactivates, and n = 0.58 during the final stages (orange dashed lines). In (b) the red curve shows the observed data, the black line shows the median stochastically-simulated model as described in Section 5.3, with the shaded region representing 95% of the models.

5.4. Assigning injection volumes to seismicity

Verdon and Budge (2018) treated each hydraulic fracturing stage as an independent event, and did not treat the volumes cumulatively as injection stages proceeded. In contrast, for the PNR-1z dataset, Figures 9 and 10 show the importance of treating multiple stages in a cumulative manner, and that failure to do so would have produced a significant underestimate of the expected event magnitudes for some stages. We believe that the difference in behaviours between the two sites stems from the orientations of the faults relative to the well trajectories. In the Horn River Basin site described by Verdon and Budge (2018), the reactivated faults were orientated roughly perpendicular to the wells. As such, each seismogenic feature was only affected by one or two stages (Kettlety *et al.*, 2019). In contrast, for PNR-1z the NEF-1 fault runs obliquely to the well, and so this feature was intersected by multiple fracture stages, hence the need to treat these stages cumulatively.

Assigning the appropriate fluid volume when making such assessments remains a challenging issue (e.g., Atkinson *et al.*, 2016). The comparison of the Horn River Basin and PNR-1z examples described above shows that detailed analysis of microseismic event locations, combined with a geomechanical understanding of the subsurface, is needed to guide such decisions.

6. Conclusions

Recent hydraulic fracturing operations at the Preston New Road PNR-1z well were subject to some of the most stringent regulations regarding induced seismicity ever applied to any kind of industrial activity. The operator therefore took a proactive approach to the issue, using real time microseismic monitoring to make operational decisions with respect to induced seismicity. Microseismic observations allowed us to identify the presence of a pre-existing structure on which elevated levels of seismicity was occurring, and to map its extent in the subsurface. This structure produced multiple events that were above the TLS red light threshold, forcing the operator to stop injection, resulting in wasted stages, where fluid injection ceased before significant quantities of proppant could be placed. Using the microseismic observations, the operator was able to move to injection locations that were less likely to interact with this structure, thereby increasing the chance of conducting successful stages.

At the same time, we used the microseismic observations to populate a statistical model to estimate an upper bound for the largest expected event size during injection. This model was successful in forecasting the magnitudes of the events that did occur. The forecast maximum magnitudes of $M_{MAX} < 2$ was within the overall objective set by the regulator to minimise the number of felt events and eliminate the possibility of damaging events. This modelling gave the operator and the regulator confidence that, even if the seismogenic structure were to be intersected by further fracturing stages, the level of risk posed was acceptable. This confidence was borne out during operations: as further activity did occur on the identified fault, but the largest event to occur had a magnitude of $M = 1.5$, within the expectations provided by the statistical model.

Various options have been suggested to regulate induced seismicity. Fault respect distances (Westwood *et al.*, 2017) require an operator to avoid known faults in the subsurface.

However, this case study, along with previous cases (e.g., Igonin *et al*., 2019; Kettlety *et al.*, 2019) shows that reactivated faults may not be visible on 3D seismic surveys, especially if they have strike slip displacement, while imaged faults may not be near to their critical stress and therefore don't reactivate. Therefore the use of fault respect distances will not provide an effective approach to induced seismicity regulation.

Whereas more advanced approaches to the mitigation of induced seismicity have been proposed (e.g., Mignan *et al.*, 2017; Verdon and Budge, 2018) and demonstrated (Kwiatek *et al.*, 2019), simple Traffic Light Schemes are the most common form of regulation applied by regulators to mitigate HF-IS. The retroactive nature of these TLSs means that red light thresholds may be set far lower than the actual level of seismicity that a regulator wishes to prevent. Decisions are based solely on the magnitude of the largest events, which is a reasonable choice if sites are monitored by regional arrays that provide limited detection thresholds and poorly-constrained event locations. However, where operators acquire high-quality real-time microseismic data, providing thousands of accurately-located events across several orders of magnitude, then a TLS that use only the largest event magnitude, and therefore discards 99.9% of the observations available, seems unnecessarily crude. In this paper we have demonstrated how an operator can use microseismicity to assess the seismic risk, and make proactive decisions to mitigate induced seismicity in real time. Such an approach is more in line with the type of goal-setting regulation (Lindøe *et al*., 2012) that has been applied with much success to other aspects of the oil and gas industry. Induced seismicity poses a risk for other forms of sub-surface industrial activity including engineered geothermal systems, and the storage of CO_2 in geologic reservoirs. As induced seismicity continues to attract public scrutiny, the proactive real-time use of seismic monitoring, as demonstrated here, could see many other applications.

Data and Resources

The event catalogues and injection data used in this paper are scheduled to be released by the Oil and Gas Authority (https://www.ogauthority.co.uk/data-centre/) on the 27th June 2019.

Acknowledgements

We would like to thank Cuadrilla Resources and their joint venture partners Spirit Energy and A J Lucas for collaboration on this project. We would like to thank the BGS for providing data from the additional surface stations that were installed at the site. We would also like to thank Schlumberger for processing the monitoring data in real time. JPV was funded by NERC Grant NE/R018162/1, TK was supported by the NERC GW4+ Doctoral Training Partnership (Grant NE/L002434/1), and JMK and AFB were funded by NERC Grant NE/R018006/1.

References

Aki K., 1965. Maximum likelihood estimate of b in the formula log $N = a - bM$ and its confidence limits: Bulletin of the Earthquake Research Institute, University of Tokyo 43, 237-239.

Akkar S., M.A. Sandikkaya, J.J. Bommer, 2014. Empirical ground-motion models for point- and extended-source crustal earthquake scenarios in Europe and the Middle East: Bulletin of Earthquake Engineering 12, 359-387.

Atkinson, G.M., D.W. Eaton, H. Ghofrani, D. Walker, B. Cheadle, R. Schultz, R. Shcherbakov, K. Tiampo, J. Gu, R.M. Harrington, Y. Liu, M. van der Baan, H. Kao, 2016. Hydraulic fracturing and seismicity in the Western Canada Sedimentary Basin: Seismological Research Letters 87, 631-647.

Baisch S., C. Koch, A. Muntendam-Bos, 2019. Traffic Light Systems: To what extent can induced seismicity be controlled: Seismological Research Letters, in press.

Bao X. and D.W. Eaton, 2016. Fault activation by hydraulic fracturing in western Canada: Science 354, 1406-1409.

Bosman K., A. Baig, G. Viegas, T. Urbancic, 2016. Towards an improved understanding of induced seismicity associated with hydraulic fracturing: First Break 34, 61-66.

Broccardo M., A. Mignan, S. Wiemer, B. Stojadinovic, D. Giardini, 2017. Hierarchical Bayesian modeling of fluid-induced seismicity: Geophysical Research Letters 44, 11,357-11,367.

Butcher A., R. Luckett, J.P. Verdon, J-M. Kendall, B. Baptie, J. Wookey, 2017. Local magnitude discrepancies for near-event receivers; implications for the UK traffic light scheme: Bulletin of the Seismological Society of America 107, 532-541.

Cuadrilla Resources Ltd., 2018. Preston New Road 1z Hydraulic Fracture Plan. Accessed at: https://consult.environment-agency.gov.uk/onshore-oil-and-gas/information-on-cuadrillas-preston-new-road-site/supporting_documents/Preston%20New%20Road%20HFP.pdf on 25/3/2019.

Chambers K., J-M. Kendall, S. Brandsberg-Dahl, J. Rueda, 2010. Testing the ability of surface arrays to monitor microseismic activity: Geophysical Prospecting 58, 821-830.

Chen X., J. Haffener, T.H.W. Goebel, X. Meng, Z. Peng, J.C. Chang, 2018. Temporal correlation between seismic moment and injection volume for an induced earthquake sequence in central Oklahoma: Journal of Geophysical Research 123, 3047-3064.

Clarke H., L. Eisner, P. Styles, P. Turner, 2014. Felt seismicity associated with shale gas hydraulic fracturing: The first documented example in Europe: Geophysical Research Letters 41, 8308-8314.

Clauset A., C.R. Shalizi, M.E.J. Newman, 2009. Power-law distributions in empirical data: Society for Industrial and Applied Mathematics Review 51, 661-703.

De Barros L., F. Cappa, Y. Guglielmi, L. Duboeuf, J-R. Grasso, 2019. Energy of injection-induced seismicity predicted from *in-situ* experiments: Nature Scientific Reports 9:4999.

Dinske C. and S. Shapiro, 2013. Seismotectonic state of reservoirs inferred from magnitude distributions of fluid-induced seismicity: Journal of Seismology 17, 13-25.

Edwards B. and J. Douglas, 2014. Magnitude scaling of induced earthquakes: Geothermics 52, 132-139.

Eyre T.S., D.W. Eaton, M. Zecevic, D. D'Amico, D. Kolos, 2019. Microseismicity reveals fault activation before M_w 4.1 hydraulic-fracturing induced earthquake: Geophysical Journal International 218, 534-546.

Fellgett M.W., A. Kingdon, J.D.O. Williams, C.M.A. Gent, 2017. State of stress across UK regions: British Geological Society, Nottingham, UK. Open File Report OR/17/048.

Friberg P.A., G.M. Besana-Ostman, I. Dricker, 2014. Characterisation of an earthquake sequence triggered by hydraulic fracturing in Harrison County, Ohio: Seismological Research Letters 85, 1295-1307.

Galis M., J.P. Ampuero, P.M. Mai, F. Cappa, 2017. Induced seismicity provides insight into why earthquake ruptures stop: Science Advances 3, eaap7528.

Green C.A., P. Styles, B.J. Baptie, 2012. Preese Hall shale gas fracturing review and recommendations for induced seismic mitigation. Department of Energy and Climate Change, London.

Grigoli F., S. Cesca, A.P. Rinaldi, A. Manconi, J.A. López-Comino, J.F. Clinton, R. Westaway, C. Cauzzi, T. Dahm, S. Wiemer, 2018. The November 2017 MW 5.5. Pohang earthquake: A possible case of induced seismicity in South Korea: Science 360, 1003-1006.

Gutenberg B., and C.F. Richter, 1944. Frequency of earthquakes in California: Bulletin of the Seismological Society of America 34, 185-188.

Hallo M., I. Oprsal, L. Eisner, M.Y. Ali, 2014. Prediction of magnitude of the largest potentially induced seismic event: Journal of Seismology 18, 421-431.

Hammack R., W. Harbert, S. Sharma, B. Stewart, R. Capo, A. Wall, A. Wells, R. Diehl, D. Blaushild, J. Sams, G. Veloski, 2014. An Evaluation of Fracture Growth and Gas/Fluid Migration as Horizontal Marcellus Shale Gas Wells are Hydraulically Fractured in Greene County, Pennsylvania: EPAct Technical Report Series, U.S. Department of Energy, National Energy Technology Laboratory, Pittsburgh, PA, NETL-TRS-3-2014.

Hansard, 2018. House of Commons Official Report 649(208), 714-716.

Häring M.O., U. Schanz, F. Ladner, B.C. Dyer, 2008. Characterisation of the Basel 1 enhanced geothermal system: Geothermics 37, 469-495.

Hofmann H., G. Zimmermann, A. Zang, K-B. Min, 2018. Cyclic soft stimulation (CSS): A new fluid injection protocol and traffic light system to mitigate seismic risks of hydraulic stimulation treatments: Geothermal Energy 6, 27.

Hofmann H., G. Zimmermann, M. Farkas, E. Huenges, A. Zang, M. Leonhardt, G. Kwiatek, P. Martinez-Garzon, M. Bohnhoff, K-B. Min, P. Fokker, R. Westaway, F. Bethmann, P. Meier, K.S. Yoon, J.W. Choi, T.J. Lee, K.Y. Kim, 2019. First field application of cyclic soft stimulation at the Pohang enhanced geothermal system site in Korea: Geophysical Journal International 217, 926-949.

Igonin N., J.P. Verdon, J-M. Kendall, D.W. Eaton, 2019. The importance of pre-existing fracture networks for fault reactivation during hydraulic fracturing: Journal of Geophysical Research, *sub judice*.

Kendall J-M., A. Butcher, A.L. Stork, J.P. Verdon, R. Luckett, B.J. Baptie, 2019. How big is a small earthquake? Challenges in determining microseismic magnitudes: First Break 37, 51-56.

Keranen K.M., M. Weingarten, G.A. Abers, B.A. Bekins, S. Ge, 2014. Sharp increase in central Oklahoma seismicity since 2008 induced by massive wastewater injection: Science 345, 448-451.

Kettlety T., J.P. Verdon, M.J. Werner, J-M. Kendall, J. Budge, 2019. Investigating the role of elastostatic stress transfer during hydraulic fracturing-induced fault reactivation: Geophysical Journal International 217, 1200-1216.

Kwiatek G., T. Saamo, T. Ader, F. Bluemle, M. Bohnhoff, M. Chendorain, G. Dresen, P. Heikkinen, I. Kukkonen, P. Leary, M. Leonhardt, P. Malin, P. Martinez-Garzon, K. Passmore, P. Passmore, S. Valenzuela, C. Wollin, 2019. Controlling fluid-induced seismicity during a 6.1-km-deep geothermal stimulation in Finland: Science Advances 5, eaav7224.

Li X., I. Main, A. Jupe, 2018. Induced seismicity at the UK 'hot dry rock' test site for geothermal energy production: Geophysical Journal International 214, 331-344.

Lindøe P.H., M. Baram, J. Paterson, 2012. Robust Offshore Risk Regulation – an assessment of US, UK and Norwegian approaches: European Safety and Reliability Conference, Helsinki.

Luckett R., L. Ottemoller, A. Butcher, B. Baptie, 2019. Extending local magnitude M_L to short distances: Geophysical Journal International 216, 1145-1156.

Maxwell S.C., J. Shemeta, E. Campbell, D. Quirk, 2008. Microseismic deformation rate monitoring: SPE Annual Technical Conference, SPE116596.

Maxwell S.C., M. Jones, R. Parker, S. Miong, S. Leaney, D. Dorval, D. D'Amico, J. Logel, E. Anderson, K. Hammermaster, 2009. Fault activation during hydraulic fracturing: SEG Annual Meeting Expanded Abstracts 28, 1552-1556.

Maxwell S.C., J. Rutledge, R. Jones, M. Fehler, 2010. Petroleum reservoir characterization using downhole microseismic monitoring: Geophysics 75, A129-A137.

Mignan A., M. Broccardo, S. Wiemer, D. Giardini, 2017. Induced seismicity closed-form traffic light system for actuarial decision-making during deep fluid injections: Nature Scientific Reports 7:13607.

Oil and Gas Authority, 2018. Consolidated Onshore Guidance, Version 2.2. Oil and Gas Authority, London. Accessed at: https://www.ogauthority.co.uk/media/4959/29112017_consolidated-onshore-guidance-compendium_vfinal-002.pdf on 5/04/2019.

Schultz R., V. Stern, M. Novakovic, G. Atkinson, Y.J. Gu, 2015. Hydraulic fracturing and the Crooked Lake sequences: Insights gleaned from regional seismic networks: Geophysical Research Letters 42, 2750-2758.

Schultz R., G. Atkinson, D.W. Eaton, Y.J. Gu, H. Kao, 2018. Hydraulic fracturing volume is associated with induced earthquake productivity in the Duvernay play: Science 359, 304-308.

Segall, P., 1989. Earthquakes triggered by fluid extraction: Geology 17, 942-946.

Shapiro S.A., C. Dinske, C. Langenbruch, 2010. Seismogenic index and magnitude probability of earthquakes induced during reservoir fluid stimulations: The Leading Edge 29, 304-309.

Skoumal R.J., M.R. Brudzinski, B. S. Currie, 2015. Induced earthquakes during hydraulic fracturing in Poland Township, Ohio: Bulletin of the Seismological Society of America 105, 189-197.

van der Elst, N.J., M.T. Page, D.A. Weiser, T.H.W. Goebel, S.M. Hosseini, 2016. Induced earthquake magnitudes are as large as (statistically) expected: Journal of Geophysical Research 121, 4575-4590.

Verdon J.P., 2014. Significance for secure CO_2 storage of earthquakes induced by fluid injection: Environmental Research Letters 9, 064022.

Verdon J.P. and J. Budge, 2018. Examining the capability of statistical models to mitigate induced seismicity during hydraulic fracturing of shale gas reservoirs: Bulletin of the Seismological Society of America 108, 690-701

Wang Z. and A. Krupnick, 2013. A retrospective review of shale gas development in the United States: What lead to the boom?: Resources for the Future DP 13-12.

Webster B., 2018. Cuadrilla to resume fracking seven years after tremors: The Times, 16th October 2018. Accessed at: https://www.thetimes.co.uk/article/cuadrilla-to-resume-fracking-seven-years-after-tremors-h6lrndhxj on 28/3/2019.

Wessels, S.A., A. De La Peña, M. Kratz, S. Williams-Stroud, T. Jbeili, 2011. Identifying faults and fractures in unconventional reservoirs through microseismic monitoring: First Break 29, 99-104.

Westwood R.F., S.M. Toon, P. Styles, N.J. Cassidy, 2017. Horizontal respect distance for hydraulic fracturing in the vicinity of existing faults in deep geological reservoirs: a review and modelling study: Geomechanics and Geophysics for Geo-Energy and Geo-Resources 3, 379-391.

Wiemer S. and M. Wyss, 2000. Minimum magnitude of completeness in earthquake catalogs: Examples from Alaska, the western United States, and Japan: Bulletin of the Seismological Society of America 90, 859-869.

Williams M.J. and J. Le Calvez, 2013. Reconstructing frequency-magnitude statistics from detection limited microseismic data: Geophysical Prospecting 61, 20-38.

Zang A., G. Zimmermann, H. Hofmann, O. Stephansson, K-B. Min, K.Y. Kim, 2019. How to reduce fluid-injection-induced seismicity: Rock Mechanics and Rock Engineering 52, 475-493.

Zinno R., J. Gibson, R.N. Walker Jr, R.J. Withers, 1998. Overview: Cotton Valley hydraulic fracture imaging project: SEG Annual Meeting Expanded Abstracts 17, 338-341.